Oxidized Late Mesozoic subcontinental lithospheric mantle beneath the eastern North China Craton: A clue to understanding cratonic destruction

Lubing Hong [a,*], Yigang Xu [a], Le Zhang [a], Zhe Liu [a,b], Xiaoping Xia [a], Yongsheng Kuang [c]

[a] State Key Laboratory of Isotope Geochemistry, Guangzhou Institute of Geochemistry, Chinese Academy of Sciences, Guangzhou 510640, China
[b] University of Chinese Academy of Sciences, Beijing 100049, China
[c] College of Minning, Inner Mongolia University of Technology, Hohhot 010080, China

ARTICLE INFO

ABSTRACT

Despite the critical influence of oxidation state on the geochemical and geodynamic evolution of Earth, its impact on the longevity of cratons is poorly understood. To address this issue, we investigated the redox state of the Late Mesozoic subcontinental lithospheric mantle (SCLM) beneath the eastern North China Craton (NCC), which was destroyed during the Phanerozoic. We report the occurrence of high-Fo olivine (Fo > 87, where Fo = atomic Mg/(Mg + Fe²⁺)) within Early Cretaceous basalts; these olivines show extremely low Ti (<60 ppm) contents, high $\delta^{18}O$ (5.8‰–7.2‰) values, and relatively cool crystallization temperatures (1125 to 1218 °C). These features support derivation of the lavas from highly refractory and cold SCLM. The relatively low partition coefficients of vanadium between olivine and whole rocks (0.019–0.025) indicate a high fO_2 for the Early Cretaceous basalts and their mantle sources ($\Delta QFM = +1.0$ and $\Delta QFM = +1.5$, respectively), and, consequently, an oxidized Late Mesozoic SCLM beneath the eastern NCC. The high degree of oxidation of the mantle was caused by the ingress of hydrous melts and/or fluids released from a subducting slab during the Phanerozoic. We propose that oxidization of the SCLM softened the mantle, which triggered the removal of the cratonic root beneath the eastern NCC. The results highlight the crucial role of oxidation state in craton stability.

© 2019 International Association for Gondwana Research. Published by Elsevier B.V. All rights reserved.

1. Introduction

Cratons are the ancient cores of continents that are typically underlain by a thick, cold, refractory subcontinental lithospheric mantle (SCLM) keel (e.g., Jordan, 1975; Lee et al., 2011; Walker et al., 1989; Peslier et al., 2010). Cratons typically formed during the Precambrian (Griffin et al., 2003), and underwent no major subsequent tectonism or magmatism. However, many studies have shown that in some circumstances, cratons can be thinned and destroyed, thereby removing >100 km of the SCLM keel (Wu et al., 2014 and references therein).

The rigidity of mantle rocks is influenced by several parameters, including chemical composition, temperature, and water content (Lee et al., 2011). In addition, redox state can influence the strength of the mantle. Studies of mantle xenoliths have shown that an intact craton is typically underlain by extremely reduced SCLM, with a reduction gradient in oxygen fugacity (fO_2) of 0.5–0.9 log units per GPa (Foley, 2011; Miller et al., 2016). Such reduction permits carbon to be stable in its native states of diamond or graphite. However, any oxidation of the mantle leads to the transformation of diamond/graphite to carbonate (Foley, 2008, 2011), thereby triggering mantle melting (Dasgupta and Hirschmann, 2006, 2010) and a reduction in rigidity as carbonate-rich partial melts percolate along grain boundaries (Foley, 2011; Gonzalez and Gorczyk, 2017; Tappe et al., 2017). In addition, recent studies have demonstrated that oxidation state can markedly influence the seismic properties of the mantle, in which increasing fO_2 leads to a decrease in wave speed and an increase in wave attenuation, which are the seismic characteristics generally associated with low-viscosity mantle (Cline et al., 2018). This observation implies that mantle oxidation can soften mantle rocks (Irifune and Ohuchi, 2018). However, to date, the role of redox state on cratonic stability has received little attention.

The North China Craton (NCC) stabilized during the Paleoproterozoic (ca. 1.9 Ga; Zhao et al., 2001) and remained stable until the late Paleozoic. Data from mantle xenoliths show that during the Middle Ordovician, the SCLM beneath the eastern NCC was cold (~40 mW/m²), thick (>180 km), ancient (>2.5 Ga), and refractory (Chu et al., 2009; Gao et al., 2002; Griffin et al., 1998; Menzies et al., 1993; Menzies and Xu, 1998; Zheng et al., 2006). In contrast, studies of Cenozoic mantle xenoliths have shown that the present-day SCLM beneath the eastern NCC is hot (60–80 mW/m²), thin (<80 km), juvenile, and fertile (e.g., Chu et al., 2009; Fan et al., 2000; Gao et al., 2002; Hong et al., 2012; Zheng et al., 2006). This distinct change in the SCLM demonstrates that at least 100 km of cratonic root beneath the eastern NCC were lost during the Phanerozoic (Griffin et al., 1998; Menzies

et al., 1993; Menzies and Xu, 1998; Xu, 2001; Zheng et al., 2006). Thus, the eastern NCC represents the best-known example of craton destruction.

The large volumes of Early Cretaceous mantle-derived lavas in the eastern NCC suggest that the destruction of the craton occurred primarily during that period (Wu et al., 2005; Xu et al., 2009; Zhu et al., 2012; Zheng et al., 2018). Studies of these lavas have shown that they originated mainly from the SCLM (Xu et al., 2009; Zheng et al., 2018; and references therein), and consequently record information on the redox state of the SCLM during the period of cratonic destruction. In this study, we investigated Early Cretaceous olivine basalts from five localities in the eastern NCC. Following the model of Canil (2002), we measured the compositions of high-Fo olivine (Fo > 87, where Fo = atomic $Mg/(Mg + Fe^{2+})$) phenocrysts, and estimated fO_2 in the magmas from which they crystallized using partition coefficients of vanadium (V) between olivine and their host whole rocks. Using these data, we reconstruct the redox state of the SCLM source of the basalts and discuss the important role of redox state on craton stability.

2. Geological background and sample descriptions

The NCC in eastern Asia is one of the oldest cratons in the world (up to 3.8 Ga; Liu et al., 1992; Zheng et al., 2004). It is separated into two Archean blocks (the Eastern and Western Blocks) along the Paleoproterozoic Trans-North China Orogen (Fig. 1; Zhao et al., 2001). The NCC is bound by three orogenic belts that formed as a result of Phanerozoic subduction: the Qilianshan Orogen to the west, the Central Asian Orogenic Belt to the north, and the Sulu–Dabie–Qiling Orogen to the south and southeast (Fig. 1).

Early Cretaceous olivine basalts from five localities in the eastern NCC were selected for investigation: the ca. 125 Ma Sihetun basalts and ca. 126 Ma Zhangwu basalts from the Yixian group in Liaoxi (Gao et al., 2008; Huang et al., 2007); the ca. 115 Ma Qingdao basalts and ca. 125 Ma Fangcheng basalts from the Qingshan group in Jiaodong Peninsula (Kuang et al., 2012) and Luxi (Zhang et al., 2002; Guo et al., 2013a; Guo et al., 2013b), respectively; and the ca. 110 Ma Fushun basalts from the Xiaoling group in Liaodong Peninsula (Pang et al., 2015; Fig. 1). These basalts, which underwent little crustal contamination, have compositions ranging from tephrite to basalt, and generally show arc-like trace-element compositions, such as depletion in fluid-immobile elements (Nb, Ta, Zr, Hf, and Ti) (Table EA1; Fig. 2), and enriched Sr–Nd isotope compositions ($\varepsilon_{Nd}(t)$ as low as −15; Kuang et al., 2012; Gao et al., 2008; Pang et al., 2015; Zhang et al., 2002; Guo et al., 2013a; Guo et al., 2013b; Huang et al., 2007). The olivine grains in these basalts are generally euhedral to subhedral and contain inclusions of spinel and melt (Qian et al., 2017; Guo et al., 2013b; Kuang et al., 2012; Gao et al., 2008; Pang et al., 2015; Huang et al., 2007).

3. Analytical methods

3.1. LA-ICP-MS analysis

Olivine grains were selected and mounted in epoxy resin disks. Olivine compositions were determined by in situ laser-ablation inductively coupled plasma mass spectrometry (LA-ICP-MS) at the Wuhan Sample Solution Analytical Technology Co., Ltd., Wuhan, China, and laser ablation-inductively coupled plasma-sector field-mass spectrometry (LA-ICP-SF-MS) at the State Key Laboratory of Isotope Geochemistry, Guangzhou Institute of Geochemistry, Chinese Academy of Sciences, Guangzhou, China. Detailed operating conditions for the laser ablation system and the ICP-MS instrument and data reduction in the LA-ICP-MS and LA-ICP-SF-MS analysis are the same as described by Zong et al. (2017) and Zhang et al. (2018), respectively. Analyses were carried out with helium as a carrier gas, and argon as the make-up gas. In the
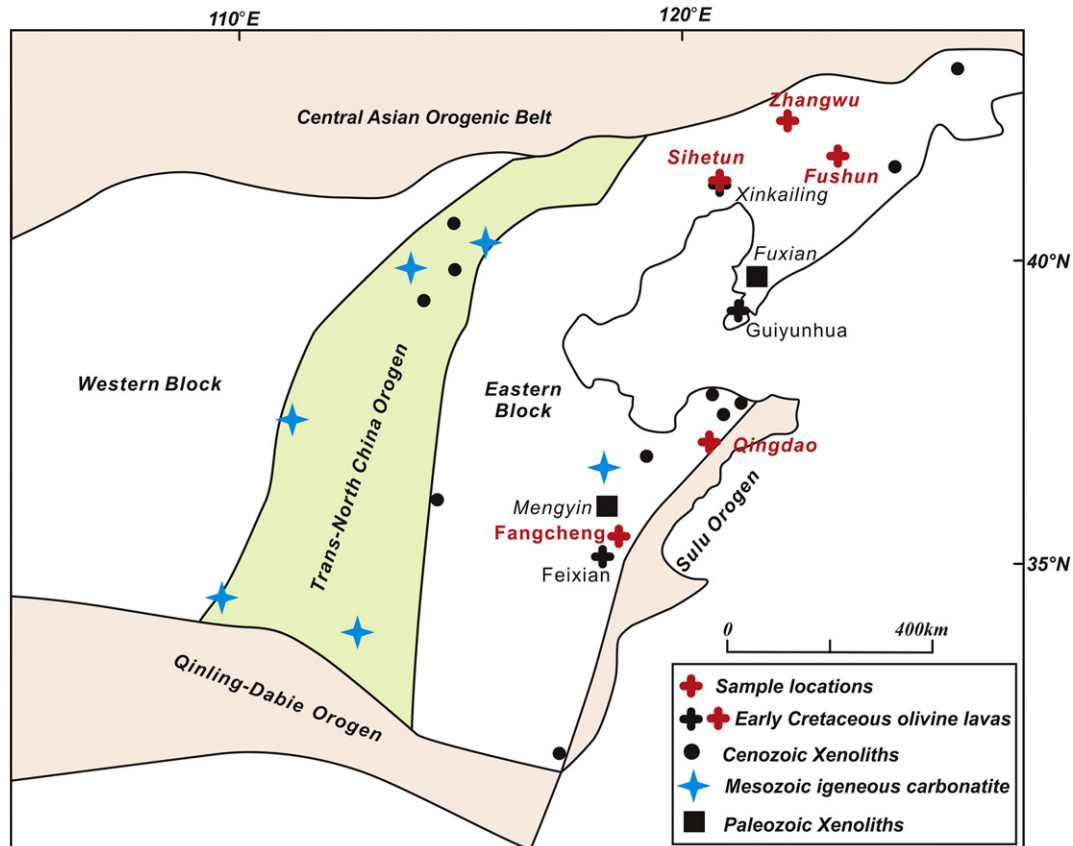
Fig. 1. Distribution of Paleozoic and Cenozoic mantle xenoliths, Mesozoic igneous carbonatites, and Early Cretaceous olivine-bearing lavas in the North China Craton. The tectonic subdivisions follow Zhao et al. (2001).
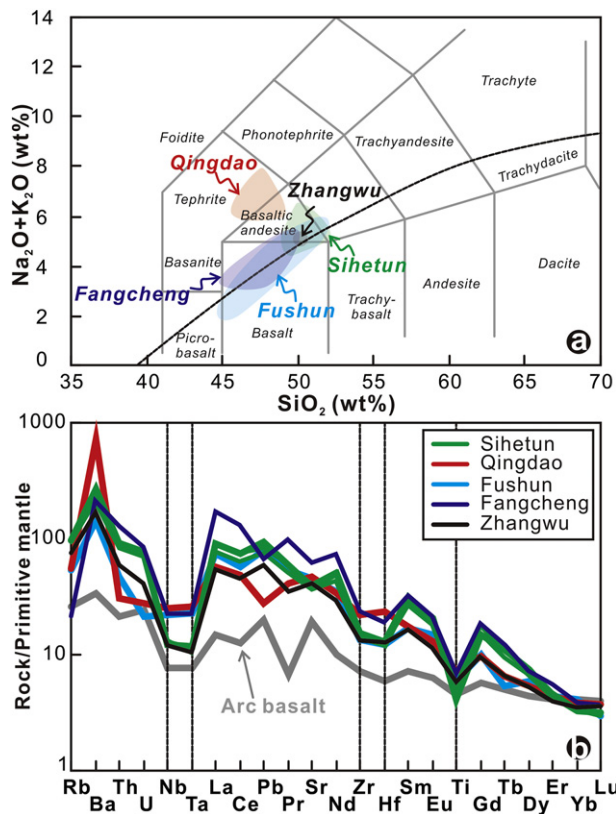
Fig. 2. TAS diagram (a) and primitive-mantle-normalized trace-element patterns (b) for Early Cretaceous basalts from the NCC. The TAS diagram follows Le Bas et al. (1986), and the normalizing values are from McDonough and Sun (1995). The composition of arc basalt in (b) is the global average of Kelemen et al., 2003.

LA-ICP-MS analysis, the spot size and frequency of the laser were set to 40 μm and 5 Hz, respectively. Olivine compositions were calibrated against various reference materials (BHVO-2G, BCR-2G and BIR-1G) with Si as an internal standard, and a reference material (NIST 610) for time-drift correction (Liu et al., 2008). Each analysis included a 20–30 s background acquisition and a 50 s data acquisition. ICPMSDataCal software was used to perform an off-line selection, the integration of background and analyzed signals, a time-drift correction and a quantitative calibration for trace element analysis (Liu et al., 2008). In the LA-ICP-SF-MS analysis, the spot size and frequency of the laser were set to 33 μm and 5 Hz, respectively. Olivine compositions were calibrated against various reference materials (BHVO-2G, BCR-2G and GSD-1G) with Mg as an internal standard. Each analysis included a 20 s background acquisition and a 30 s data acquisition. A MATLAB program named TraceElement was used to perform an off-line selection, the integration of background and analyzed signals, and a quantitative calibration for the analysis (Zhang et al., 2018). The precisions of all reported elements in olivines were better than 10%.

3.2. SIMS analysis

The olivine grains analyzed by LA-ICP-MS were remounted in epoxy together with the Jingyu olivine standards (06JY29; Su et al., 2015) from North China and the San Carlos olivine standards. Olivine oxygen isotope compositions were analyzed in situ by a Cameca IMS 1280-HR secondary ion mass spectrometer (SIMS) at the State Key Laboratory of Isotope Geochemistry, Guangzhou Institute of Geochemistry, Chinese Academy of Sciences, following the same analytical procedures described by Yang et al. (2018). Olivines were sputtered with a 10 kV Cs^+ primary beam of 2–3 nA current focused to ~10 μm spots after a pre-sputtering time of 35 s with a 20 μm square raster. A single spot

analysis lasted for 3 min, in which 2 min was used for pre-sputtering and automatic centering in the secondary optics, and 1 min was used for integrating 16 cycles of the oxygen isotope signal. Corrections for instrumental mass fractionation (IMF) were conducted by a "standard-sample-standard" bracketing external standardization method. The 06JY29 olivines were used as the external standard and the San Carols olivines were used as unknowns. Each 06JY29 olivine analysis was conducted with every five unknown spots in the whole session. The $^{18}O/^{16}O$ ratios were normalized to Vienna Standard Mean Ocean Water (V-SMOW $^{18}O/^{16}O = 0.0020052$; Baertschi, 1976) and expressed on the $\delta^{18}O$-scale. A recommended value of $\delta^{18}O = 5.30 \pm 0.10‰$ (2SD) assigned to the 06JY29 olivines was used in this study, and then corrected for the IMF ($\delta^{18}O_{measured}$-$\delta^{18}O_{true}$). The internal precision is within 0.34‰ (2SD), and the external reproducibility of the San Carlo olivines was better than 0.36‰ (2SD). Because there is no systematic difference in the $\delta^{18}O$ IMF value obtained by SIMS for olivine with Fo > 70 (e.g., Guo et al., 2013a), and the olivines of the Early Cretaceous basalts in the NCC in this study have high Fo values (Fo > 87), we did not consider the potential matrix effects below.

4. Results

4.1. Olivine chemistry

The chemical compositions of olivine in the Early Cretaceous basalts from the eastern NCC are summarized in Table EA2, with mean values listed in Table 1. The olivine grains have high Fo values (87.0–91.8) and Ni contents (1840–4070 ppm), with the highest Fo values occurring in the Sihetun and Fangcheng basalts. They generally have low Ca (780–1490 ppm), Ti (15–56 ppm), and V (2.7–4.9 ppm) contents. The Ca contents are slightly higher than in typical mantle olivine (Ca < 715 ppm, corresponding to 0.1 wt% CaO; Thompson and Gibson, 2000), which, together with the euhedral and subhedral crystal shapes and melt/spinel inclusions, argue for a magmatic origin. The 100Mn/Fe and 100Ca/Fe ratios are 1.26–1.56 and 0.92–1.79, respectively. At a given value of 100Mn/Fe, the olivine grains generally have a much lower 100Ca/Fe ratio than non-subduction-related olivine but are comparable with olivine from convergent margins (Fig. 3b).
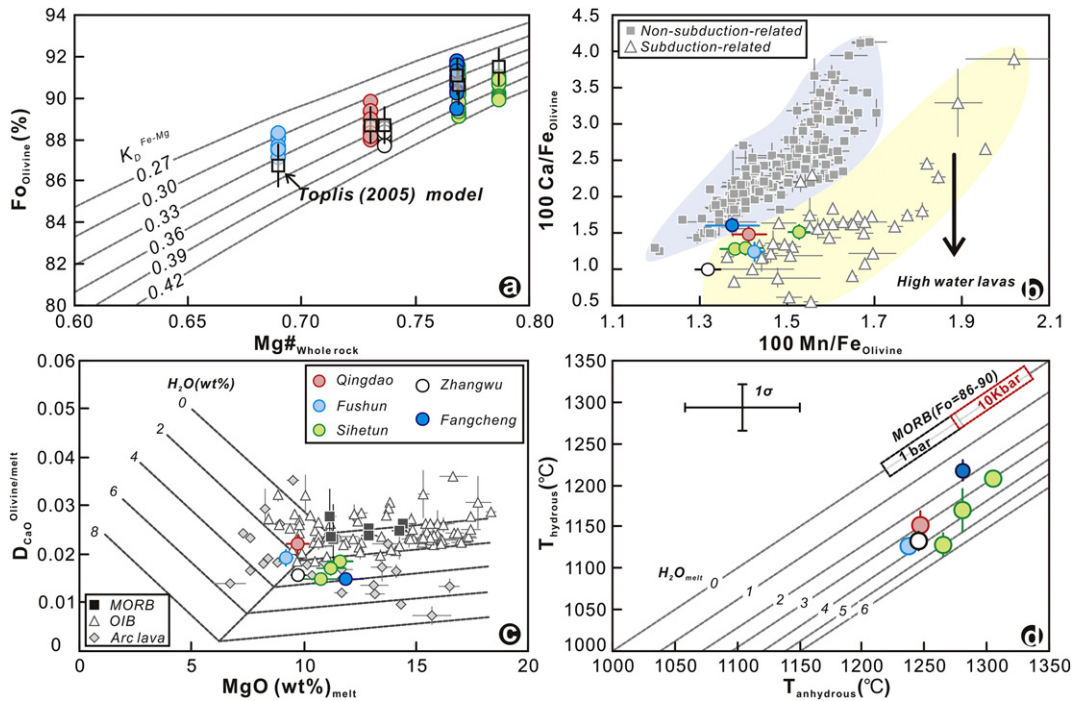
The olivine grains in the Early Cretaceous basalts have high O isotopic compositions ($\delta^{18}O_{olivine}$ = 5.8‰–7.2‰) that are similar to those of Early Cretaceous mantle olivine from the eastern NCC and from arc-related lavas (Fig. 4). The $\delta^{18}O_{olivine}$ values are substantially higher than those of olivines in mid-ocean ridge basalts (MORBs), and HIMU ocean-island basalts (OIBs) ($\delta^{18}O_{olivine}$ < 5.4‰), and partially overlap with, but are slightly higher than, $\delta^{18}O_{olivine}$ values of enriched mantle (EM) OIBs (Fig. 4).

4.2. Oxygen fugacity

The partition coefficients for Fe and Mg (K_D^{Fe-Mg}) between olivine and whole rocks in the Early Cretaceous basalts range from 0.30 to 0.42 (Fig. 3a). This range is broadly consistent with the values predicted by the model of Toplis (2005) (Fig. 3a), suggesting equilibrium. As Fo values of all of the analyzed olivine grains are high (>87), and similar to those from the mantle-derived primary magmas, we assume that the Early Cretaceous basalts represent primary magmas.

Partition coefficients for V (D_V) in the Early Cretaceous basalts, which were obtained from the measured V contents of olivine divided by those in the whole rocks, range from 0.019 ± 0.002 to 0.025 ± 0.002 (Table 1). Using the model of Canil (2002), we calculated the oxygen fugacity relative to the quartz–fayalite–magnetite buffer (ΔQFM) in the Early Cretaceous basalts at 1 atm as lying between 0.79 ± 0.15 and 1.21 ± 0.13 (Table 1).

For comparison, we compiled fO_2 values for a global dataset of lavas based on the D_V and $Fe^{3+}/\Sigma Fe$ data. For the D_V dataset, the procedure for obtaining fO_2 values was the same as that used for the Early Cretaceous

Fig. 3. Geochemical plots for the Early Cretaceous basalts, North China Craton. (a) Fe/Mg equilibrium between olivines ($Fo_{olivine}$) and their whole rocks ($Mg\#_{whole\ rock}$). (b) Ca/Fe (100 Ca/$Fe_{olivine}$) and Mn/Fe (100 $Mn/Fe_{olivine}$) in olivine grains. (c) Partition coefficient of Ca between olivine and whole rocks ($D_{CaO}^{olivine/melt}$) and MgO contents in equilibrium melts (MgO_{melt}). (d) Olivine crystallization temperature under hydrous ($T_{hydrous}$) and anhydrous ($T_{anhydrous}$) conditions. The high-precision data from olivine from non-subduction-related and subduction-related lavas in (b) are from the Georoc database (http://georoc.mpch-mainz.gwdg.de/georoc/), for which only the highest Fo olivine grains (typically ΔFo < 0.5) were selected. The effects of water on depression of $D_{CaO}^{olivine/melt}$ values in (c) and on depression of olivine liquidus temperature in (d) follow Gavrilenko et al. (2016) and Médard and Grove (2008), respectively (see Section 4.3 in text for details).

basalts described above. Like the Early Cretaceous basalts, we assumed that the lavas in equilibrium with high-Fo (>86) olivine represent primary magmas. For low-Fo (<86) olivine, we reconstructed fO_2 values of the primary magmas by sequentially adding 0.01% olivine with an equilibrium composition until the magmas equilibrated with Fo_{90} olivine at 1 atm. These calculations were performed with Petrolog software (Danyushevsky and Plechov, 2011) using the K_D^{Fe-Mg} model of Toplis (2005), the model describing melt oxidation state of Kress and Carmichael (1988), and by assuming a closed system for oxygen. For the $Fe^{3+}/\Sigma Fe$ dataset, samples showing significant degrees of S degassing were first excluded, then fO_2 values of the global lavas were calculated with Petrolog using the Kress and Carmichael (1988) model for melt oxidation at 1 atm. The procedure for obtaining fO_2 values of the primary magmas was the same as that described for low-Fo olivine.

fO_2 values of the primary magmas of the global lavas at 1 atm are listed in Tables EA3 and EA4. fO_2 values of the primary magmas obtained using the two different datasets are identical within uncertainty (e.g., MORBs in the Siqueiros segment; Fig. 5), consistent with the conclusion of Kelley and Cottrell (2012). The studied Early Cretaceous basalts have much higher fO_2 values (ΔQFM = +1.0) compared with MORBs (ΔQFM = −0.2 to +0.5) and OIBs (ΔQFM = −0.6 to +0.7), but slightly lower values compared with arc-related lavas (ΔQFM = +0.03 to >+2.0) and ultramafic lamprophyres formed during cratonic thinning or destruction (ΔQFM = −0.15 to +1.88), which show large fO_2 ranges (Fig. 5).

4.3. Water contents

Water contents of the Early Cretaceous basalts and global lavas were determined using the Ca-in-olivine geohygrometer (Gavrilenko et al., 2016). First, we modeled olivine-controlled fractionation taking the starting compositions of the whole rocks and using Petrolog software (Danyushevsky and Plechov, 2011), the K_D^{Fe-Mg} model of Toplis (2005),

and the assumption of a closed system for oxygen. MgO and CaO contents of the melts at given Fo values were obtained by regression based on the relationships between MgO and CaO in the melt and the Fo of olivine in equilibrium with the melt. Applying the model of Gavrilenko et al. (2016), we calculated the partition coefficient values of Ca under dry ($D_{Ca}^{anhydrous}$) and hydrous ($D_{Ca}^{hydrous}$) conditions (where $\Delta D_{Ca} = D_{Ca}^{anhydrous} - D_{Ca}^{hydrous}$), and finally the water contents of the melts. Results are displayed in Tables 1 and EA2. The $D_{Ca}^{hydrous}$ and $D_{Ca}^{anhydrous}$ values of the Early Cretaceous basalts are 0.0149 ± 0.0009 to 0.0221 ± 0.0019, and 0.0245 ± 0.0002 to 0.0323 ± 0.0015, respectively. The corresponding ΔD_{Ca} values are 0.0059 ± 0.0011 to 0.0143 ± 0.0015 (Fig. 3c), and the water contents are 1.5 ± 0.5 wt% to 3.9 ± 0.5 wt% (Figs. 3c, 6).

To test the reliability of these results, we used an independent method built on the effect of water on olivine liquidus depression. We calculated the crystallization temperature of olivine under dry ($T^{anhydrous}$) and hydrous ($T^{hydrous}$) conditions using a thermometer based on the MgO content of melt (Herzberg and Asimow, 2015) and the partition coefficient for Ni between olivine and melt (Pu et al., 2017). MgO contents of the melts were assumed to be the same as those in the whole rocks, whereas Ni contents were calculated using a regression based on the Fo–Ni relationship to correct these contents with respect to the Fo values of olivine in equilibrium with the whole rocks. After obtaining $T^{hydrous}$ and $T^{anhydrous}$, we calculated ΔT (=$T^{anhydrous} - T^{hydrous}$), and the water content of the melt following the method of Médard and Grove (2008). Results are summarized in Tables 1 and EA2. The $T^{hydrous}$ and $T^{anhydrous}$ values of the Early Cretaceous basalts range from 1125 ± 6 to 1218 ± 12 °C, and from 1238 to 1306 °C, respectively. The ΔT values are 63 ± 12 to 137 ± 14 °C, and the water contents are 1.8 ± 0.4 wt% to 5.1 ± 0.9 wt% (Fig. 3d). These values are identical within uncertainty for the two independent methods: 0.7 wt% H_2O using the Ca-in-olivine geohygrometer of Gavrilenko (et al., 2016), and 41 °C and 29 °C using the models of Herzberg and Asimow (2015) and Pu et al. (2017), respectively.

Table 1

Average olivine compositions, oxygen fugacity, water contents and olivine crystallization temperature of the Early Cretaceous basalts in eastern NCC.

Sample name		Fushun	+/−	Qingdao	+/−	Fangcheng	+/−	Sihetun						Zhangwu	+/−
		FS-24	+/−	QD-2	+/−	FC09	+/−	SHT-21	+/−	SHT17–02	+/−	SHT1701	+/−	ZW06	+/−
Olivine chemistry	Fo (%)	87.60	0.37	88.65	0.52	91.00	0.60	90.91	0.43	90.50	0.42	90.03	0.65	88.20	0.32
	Fe/ppm	96,393	3051	86,717	3762	70,207	3987	71,143	3205	72,737	3156	75,463	4784	90,038	2460
	Mg/ppm	296,452	3288	294,715	4651	309,071	6347	309,573	5990	301,515	2017	296,637	2835	292,759	1437
	Ca/ppm	1197	122	1278	113	1122	94	1075	64	957	86	963	73	895	53
	Ti/ppm	40	2	49	4	29	3	27	1	32	5	21	2	28	4
	V/ppm	4.64	0.19	3.89	0.46	4.07	0.39	3.47	0.33	3.75	0.37	3.20	0.29	4.01	0.33
	Ni/ppm	2828	359	3006	358	2414	314	3355	395	3679	268	3302	507	3529	213
	Mn/ppm	1373	50	1225	65	959	82	1087	61	1039	51	1042	82	1187	25
	100Mn/Fe	1.42	0.02	1.41	0.04	1.36	0.05	1.53	0.02	1.43	0.02	1.38	0.03	1.32	0.03
	100Ca/Fe	1.24	0.13	1.47	0.12	1.60	0.11	1.51	0.10	1.31	0.09	1.28	0.06	0.99	0.05
	$\delta^{18}O$/‰	6.28	0.17	6.08	0.22	6.79	0.29	6.67	0.27	6.35	0.29				
	2σ	0.20	0.05	0.21	0.05	0.22	0.04	0.21	0.04	0.22	0.03				
Oxygen fugacity	D_V	0.021	0.001	0.022	0.003	0.025	0.002	0.021	0.002	0.024	0.002	0.019	0.002	0.023	0.002
	$\Delta QFM_{1\ atm}$[a]	1.03	0.06	0.97	0.18	0.79	0.15	1.05	0.14	0.85	0.14	1.21	0.13	0.92	0.12
	ΔQFM_{source}[b]	1.54	0.06	1.48	0.18	1.30	0.15	1.56	0.14	1.36	0.14	1.72	0.13	1.43	0.12
Water in magma 1	MgO′/wt%[c]	9.23	0.36	9.71	0.49	12.20	0.86	11.62	0.58	11.52	0.57	10.78	0.82	9.77	0.32
	CaO′/wt%[c]	8.66	0.08	8.09	0.10	10.54	0.24	8.08	0.13	7.87	0.12	9.06	0.18	7.99	0.07
	$D_{Ca}^{hydrous}$[d]	0.0193	0.0019	0.0221	0.0019	0.0149	0.0011	0.0186	0.0011	0.0170	0.0014	0.0149	0.0009	0.0157	0.0009
	$D_{Ca}^{anhydrous}$[d]	0.0323	0.0015	0.0302	0.0021	0.0247	0.0004	0.0245	0.0002	0.0248	0.0004	0.0263	0.0026	0.0300	0.0014
	ΔD_{Ca}[d]	0.0130	0.0017	0.0081	0.0024	0.0098	0.0013	0.0059	0.0011	0.0078	0.0014	0.0114	0.0020	0.0143	0.0015
	H_2O/wt%[e]	2.4	0.3	1.5	0.5	3.9	0.5	2.3	0.4	2.6	1.0	3.2	0.8	2.8	0.6
Water in magma 2	Ni′$_{olivine}$[e]	2810	76	3135	239	2197	109	3355	395	4230	95	3319	218	3568	189
	$D_{Ni'}$[f]	15.8	0.4	14.2	1.1	9.47	0.47	13.0	1.5	10.45	0.23	15.61	1.03	15.90	0.84
	T1/°C[g]	1238		1247		1281		1281		1306		1265		1246	
	T2/°C[g]	1125	6	1152	17	1218	12	1169	26	1207	5	1128	14	1133	11
	ΔT/°C[g]	112	6	95	17	63	12	112	26	98	5	137	14	112	11
	H_2O/wt%[h]	3.7	0.3	3.0	0.7	1.8	0.4	3.8	1.2	3.1	0.2	5.1	0.9	3.7	0.5

[a] Oxygen fugacity values in magmas ($\Delta QFM_{1\ atm}$) were calcualted based on Canil (2002) at 1 atm and 1200 °C, and partition coefficient of V between bulk rocks and olivines (D_V) were obtained by simply assuming the V contents in the bulk rocks as that in the magmas.

[b] Oxygen fugacity values in the mantle source (ΔQFM_{source}) were calculated by assuming at 3.0 GPa and increasing 0.17 log unit per GPa relative to QFM (see detail in text).

[c] MgO′ and CaO′ are MgO and CaO contents in the magmas which are in equilibrium with the olivine's Fo values; They were obtained by olivine fractionation modeling at the start compositions of the bulk rocks, using the K_D^{Fe-Mg} of Toplis (2005) and fO_2 obtained by D_V.

[d] Water in the magmas were calculated following the work of Gavrilenko et al. (2016); $D_{Ca}^{hydrous}$ and $D_{Ca}^{anhydrous}$ are partition coefficient of Ca between olivine and melt at hydrous and dry conditions; $D_{Ca}^{anhydrous}$ was calculated following the work of Gavrilenko et al. (2016) and $D_{Ca}^{hydrous} = Ca_{olivine}/CaO'$; $\Delta D_{Ca} = D_{Ca}^{anhydrous} - D_{Ca}^{hydrous}$.

[e] Ni′$_{olivine}$ is the Ni cotent in the olivine, which was been corrected in equilibrium with bulk rock compositions based on the relationship between MgO′ and Ni in olivine phenocrysts.

[f] $D_{Ni'} = Ni'_{olivine}/Ni_{bulk\ rock}$.

[g] T1-Olivine crystallization temperature calculated following the method of Herzberg and Asimow (2015) and using the MgO content in bulk rock; It represents the dry conditions. T2-Olivine crystallization temperature calculated based on the model of Pu et al. (2017) and using $D_{Ni'}$ listed in Table 1; it seems independent on water in the melt (Pu et al., 2017), thus, represent the hydrous condition.

[h] Water in the melts were calculated following the model of Médard and Grove (2008).
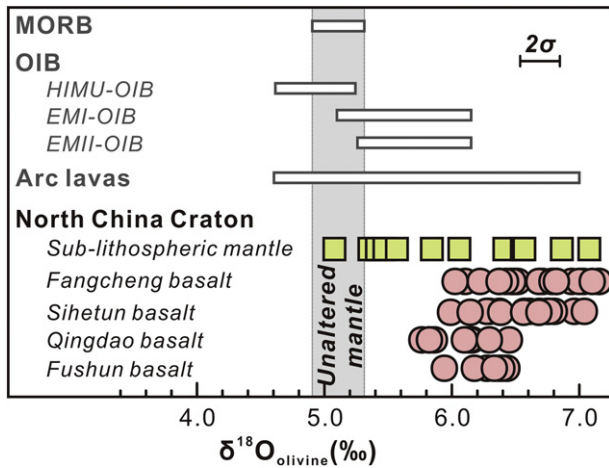
Fig. 4. Comparison of the O isotopic composition of olivine ($\delta^{18}O_{olivine}$) between the Early Cretaceous basalts and a global dataset of lavas. $\delta^{18}O_{olivine}$ data sources: MORBs and OIBs from Eiler (2001); arc lavas from Bindeman et al. (2005); $\delta^{18}O_{olivine}$ in Mesozoic SCLM from Wang et al. (2018) and Xu et al. (2013); $\delta^{18}O_{olivine}$ in Early Cretaceous basalts from Guo et al. (2013b) and this study. The range of $\delta^{18}O_{olivine}$ in unaltered mantle is defined by the MORB data.

Water contents of the Early Cretaceous lavas from the eastern NCC are higher (1.5–3.9 wt% H_2O) than those of MORBs (0–0.5 wt% H_2O), overlap with, but are slightly higher than, those of OIBs (0–2.5 wt% H_2O), and are comparable with those of arc-related lavas (1.3–7.5 wt% H_2O) (Fig. 6).

5. Discussion

5.1. Redox state of Late Mesozoic SCLM beneath the eastern NCC

5.1.1. SCLM source of the Early Cretaceous basalts

There are distinct geochemical differences between Early Cretaceous and Late Cretaceous to Cenozoic mantle-derived lavas in the eastern NCC. The Early Cretaceous lavas generally show low $\varepsilon_{Nd}(t)$ values (<0), whereas Late Cretaceous to Cenozoic lavas commonly exhibit higher $\varepsilon_{Nd}(t)$ values (>0) (e.g., Xu, 2001; Zheng et al., 2018; and references therein). These temporal and compositional differences are generally attributed to a change in source from enriched SCLM to asthenospheric mantle (Xu, 2001; Zheng et al., 2018).
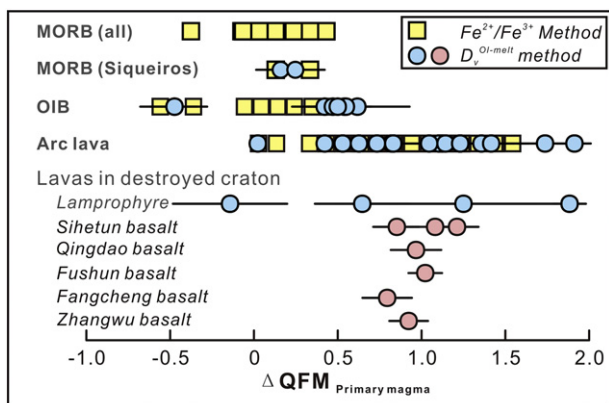
Fig. 5. Comparison of calculated oxygen fugacity relative to the QFM buffer in the primary magmas ($\Delta QFM_{primary\ magma}$) between the Early Cretaceous basalts and lavas from other areas. The $\Delta QFM_{primary\ magma}$ data are listed in Tables 1 and EA2–EA4 (see Section 4.2 for details). The lamprophyres are ultramafic lamprophyres from the Labrador Sea, the Lambert–Amery rift, and the western East African Rift, all of which formed within thinned/destroyed cratons (Foley, 2008).
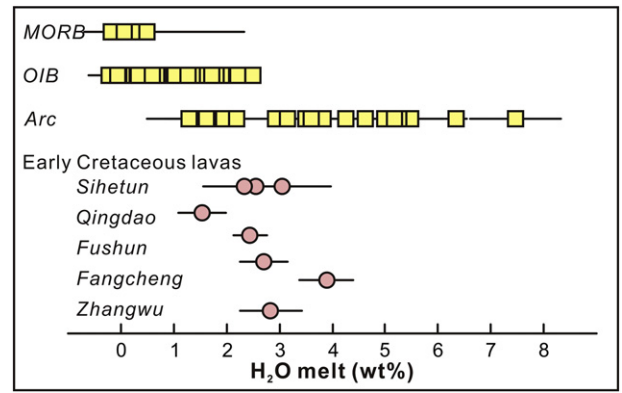
Fig. 6. Comparison of water contents of Early Cretaceous basalts from the eastern NCC with a global database of mantle-derived lavas. The water contents of the lavas (Tables 1 and EA5) were calculated using the calcium-in-olivine geohygrometer of Gavrilenko et al. (2016).

The low $\varepsilon_{Nd}(t)$ values in the Early Cretaceous basalts investigated here (−14 to −2; Table EA1; Pang et al., 2015; Kuang et al., 2012; Zhang et al., 2002; Guo et al., 2013a; Guo et al., 2013b; Huang et al., 2007; Gao et al., 2002) indicate an enriched SCLM source. Moreover, olivine grains in the Early Cretaceous basalts have extremely low Ti (<60 ppm), a feature commonly observed in partial melts of highly refractory SCLM (e.g., lamproites in orogenic belts; Foley et al., 2013). In addition, the Early Cretaceous basalts have low olivine crystallization temperatures of 1125–1218 °C (Table 1; Fig. 3d), slightly lower than those from asthenospheric mantle at the appropriate Fo values (>86), which are 1200–1320 °C according to the global MORB database (Fig. 3d). This suggests that the Early Cretaceous basalts originated from a colder mantle. Furthermore, the Early Cretaceous basalts have high $\delta^{18}O$ values (5.7‰–7.2‰; Guo et al., 2013b; this study) that are consistent with the high $\delta^{18}O$ of SCLM beneath the NCC based on the composition of contemporaneous mantle xenoliths (up to >7.0‰; Fig. 4; Wang et al., 2018; Xu et al., 2013). All of these results suggest that the investigated Early Cretaceous basalts are partial melts of enriched SCLM.

5.1.2. Oxidation state of the mantle source of the Early Cretaceous basalts

Melting temperature and pressure in the mantle may influence fO_2 in the mantle when deduced from fO_2 values of the primary magmas at 1 atm. At constant pressure, an increase in temperature can lead to a decrease in the fO_2 of silicate liquid, but the change in ΔQFM is negligible (for example, <0.02 log units from 1200 to 1400 °C at 1 GPa; Kress and Carmichael, 1991; Brounce et al., 2017). In contrast, the effect of pressure on ΔQFM is not negligible. The ΔQFM of silicate liquid increases slightly with increasing pressure at a rate of ~ 0.17 log units per GPa (Kress and Carmichael, 1991). Given the above, we corrected only for pressure to obtain ΔQFM values of the mantle source.

Early Cretaceous basalts of the NCC show weak to strong fractionation of heavy rare-earth elements, with primitive-mantle-normalized Dy/Yb ratios (Dy_{PM}/Yb_{PM}) ranging from 1.4 in the Qingdao basalts to 2.3 in the Sihetun basalts (Fig. 2b). This indicates the presence of garnet in their mantle sources, for which melting pressures of ≥~3.0 GPa may be inferred. A similar pressure (3–4 GPa) has been inferred for the source of the Sihetun basalts based on phase diagram considerations (Gao et al., 2008). Here, we assumed a melting pressure of 3.0 GPa, which likely represents minimum depths and corresponds to minimum fO_2 values of the source (Kress and Carmichael, 1991). To better understand the redox state of the mantle, we also undertook calculations on mantle-derived lavas from other localities, assuming pressures as follows: ~1.0 GPa for MORBs (e.g., Cottrell and Kelley, 2011), ~2.0 GPa for arc lavas (e.g., Lee et al., 2009; Plank and Forsyth, 2016; Gazel et al., 2012), ~3.0 GPa for OIBs (Canary and Hawaii Islands; Herzberg, 2011),

and ~5.0 GPa for ultramafic lamprophyres from thinned or destroyed regions within cratons (Foley et al., 2009).

Calculated fO_2 values of the mantle sources are given in Tables 1, EA3, and EA4. fO_2 values of the mantle source regions of the five Early Cretaceous basalts in the eastern NCC are similar, with ΔQFM around +1.5. These values are much higher than those of MORB sources (ΔQFM = −0.1 to +0.6), slightly higher than OIB sources (ΔQFM = −0.1 to +1.1), and within the range of the sources of arc lavas and ultramafic lamprophyres (ΔQFM = +0.3 to +2.5 and +0.7 to +2.7, respectively) (Fig. 7).

In contrast to the redox state of the mantle source, which is inferred based on the composition of basalts, the redox state of the SCLM is generally reconstructed using mantle xenoliths (Foley, 2011). A recent experimental study has demonstrated that for equilibrated mantle minerals and basaltic melts, absolute fO_2 values calculated using Fe^{3+}/ΣFe in basaltic melt and spinel oxybarometry show good correspondence (Davis and Cottrell, 2018), thus, confirming that there is no systematic discrepancy between absolute fO_2 values inferred from studies of basalts and mantle xenoliths. The redox state of the cratonic root reconstructed using garnet-bearing mantle xenoliths is highly reduced (ΔQFM below −1), with a reduction gradient of 0.5–0.9 log units/GPa (Foley, 2011; Miller et al., 2016). These conditions are two log units lower than those of the mantle sources of Early Cretaceous basalts in the eastern NCC (Fig. 8), indicating that these basalts were derived from an oxidized SCLM source.

5.1.3. Mantle oxidation and carbonatite magmatism

High fO_2 in the SCLM results in the transformation of diamond/graphite to carbonate, inducing mantle melting and the formation of carbonate-rich melts. Calculated fO_2 values for the Late Mesozoic SCLM beneath the eastern NCC lie above the enstatite-magnesite-olivine-graphite/diamond (EMOG/D) oxygen buffer, which defines the stability field between diamond/graphite and magnesite in cratonic SCLM (Fig. 8). This suggests that oxidization of carbon in the SCLM beneath the eastern NCC occurred during the Early Cretaceous or earlier. Support for this argument comes from the occurrence of Mesozoic igneous carbonatites that crop out in the NCC (Fig. 1; Yan et al., 2007; Ying et al., 2004). Importantly, not all carbonate-rich melts will reach the surface but may react with mantle rocks and be consumed within the SCLM. Such a scenario is consistent with the high Ca/Al and low Ti/Eu ratios of clinopyroxene grains in coeval peridotite xenoliths in the eastern NCC (Xu et al., 2013; Zhou et al., 2012; Zong and Liu, 2018).
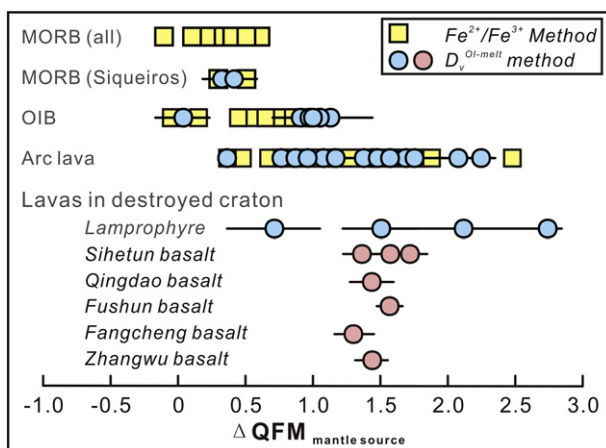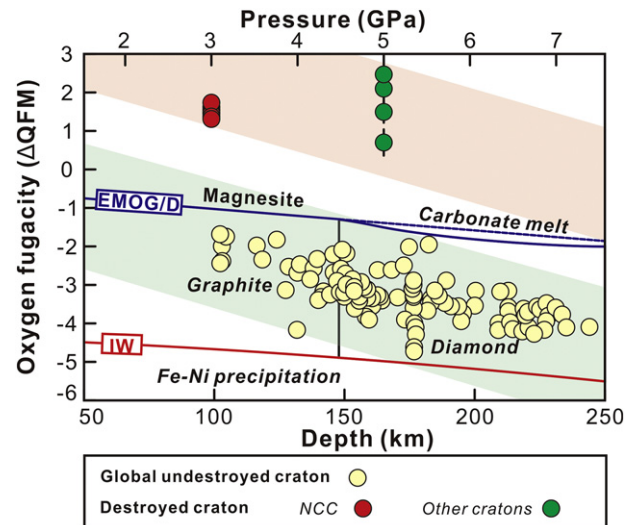

Fig. 8. Variation in oxygen fugacity of the mantle relative to the QFM buffer as a function of pressure. The ΔQFM profile of the mantle was reconstructed by assuming a reducing gradient of 0.7 log units per GPa (Foley, 2011). Curves for the EMOG/D and IW buffers are from Stagno et al. (2013). The ΔQFM values of intact cratons globally are inferred from kimberlite-bearing garnet peridotites (Foley, 2011). The ΔQFM values of destroyed cratons are inferred from Early Cretaceous basalts for the NCC and ultramafic lamprophyres for other cratons. The red and green fields indicate variations in fO_2 of destroyed and intact cratons, respectively, as a function of pressure.

5.2. Why is the oxygen fugacity of Late Mesozoic SCLM beneath the eastern NCC so high?

Cratonic roots typically have low fO_2 (down to ΔQFM = −4; Foley, 2011; Miller et al., 2016), conditions under which carbon/graphite remains stable (Fig. 8). Therefore, although the precise redox state of the SCLM beneath the eastern NCC before its destruction remains unconstrained, the presence of diamond in Middle Ordovician kimberlites (e.g., Wang et al., 1998) indicates that the SCLM was reduced (ΔQFM < −1; Stagno et al., 2013). As the SCLM was oxidized during the Late Mesozoic, as revealed by the Early Cretaceous basalts (Fig. 8), this oxidization must have occurred during the Phanerozoic.

Studies of arc-related lavas and peridotites at convergent margins have shown that fluids and/or melts released from the subducting slab are oxidized (e.g., Brounce et al., 2014, 2015; Kelley and Cottrell, 2012; Gazel et al., 2012; Plank and Forsyth, 2016; Rielli et al., 2018). Incorporation of these fluids/melts can elevate fO_2 in the mantle wedge by up to four log units above the QFM buffer (Foley, 2011; Rielli et al., 2018). These observations demonstrate that subduction is an efficient means of oxidizing the mantle (Rielli et al., 2018). There is evidence for multiple Phanerozoic subduction zones around the eastern NCC, including subduction of Paleozoic Paleo-Asian oceanic lithosphere at its northern margin, deep subduction of Yangtze continental crust during the Triassic that followed subduction of Paleo-Tethys oceanic lithosphere during the Phanerozoic at its southern margin, and Mesozoic subduction of the Paleo-Pacific plate on its eastern side (Windley et al., 2010). Three lines of evidence also suggest that subduction processes modified the Late Mesozoic SCLM of the eastern NCC: (1) Early Cretaceous lavas derived from the SCLM are generally depleted in fluid-immobile elements (Nb, Ta, and Ti) (e.g., Fig. 2b; Zheng et al., 2018, and references therein), which are characteristics of arc lavas; (2) petrological methods have revealed high water contents in Early Cretaceous lavas (1.5–3.9 wt%; Xia et al., 2013; Ma et al., 2016; Hong et al., 2017; this study), indicating a hydrated SCLM; and (3) olivine grains in the Early Cretaceous basalts and mantle xenoliths show that the SCLM in the Mesozoic had high $\delta^{18}O$ values ($\delta^{18}O$ up to 7.2‰; Fig. 4; Guo et al., 2013b; Wang et al.,

Fig. 7. Comparison of the reconstructed oxygen fugacity relative to the QFM buffer in the mantle source (ΔQFM$_{source}$) between the Early Cretaceous basalts from the NCC and lavas from other areas. The ΔQFM$_{source}$ data are given in Tables 1 and EA2–EA4 (see Section 5.1.2 for details).

2018; Xu et al., 2013; this study), consistent with mantle modified by high-$\delta^{18}O$ hydrous melts/fluids released from subducted oceanic lithosphere and/or continental crust (e.g., Bindeman et al., 2005). Therefore, we suggest that Phanerozoic subduction controlled the oxidation state of the SCLM beneath the eastern NCC during the late Mesozoic. This inference implies a protracted gradual oxidation of the SCLM beneath the eastern NCC, consistent with mantle xenoliths from the region that underwent secular carbonate metasomatism from the Late Paleozoic (Zong and Liu, 2018).

5.3. Mantle oxidation and cratonic destruction

The mechanism of destruction of the eastern NCC has been debated for several decades (Zhu et al., 2012; Wu et al., 2014 and references therein). Our results show that the SCLM of the eastern NCC was oxidized contemporaneously with its thinning and ultimate destruction. This oxidation had two consequences, both of which facilitated cratonic instability. First, mantle oxidation can soften mantle rocks, weakening the rigidity of cratons (Cline et al., 2018; Irifune and Ohuchi, 2018). Under more oxidizing conditions, ferric iron (Fe^{3+}) and associated vacancies on the metal sites in olivine would become stabilized, resulting in increased crystal defects and/or modified grain boundaries (Cline et al., 2018). Such changes would reduce the effective grain-boundary viscosity of olivine and consequently of the SCLM as a whole (Cline et al., 2018; Irifune and Ohuchi, 2018). Second, high fO_2 in the mantle likely triggers oxidation of carbon, transforming diamond/graphite into carbonate (Foley, 2008, 2011), which depresses the mantle solidus (Dasgupta and Hirschmann, 2006, 2010), triggering partial melting. The subsequent percolation of carbonate-rich partial melts along grain boundaries would decrease the rigidity of the mantle (Foley, 2008, 2011; Gonzalez and Gorczyk, 2017; Tappe et al., 2017).

Oxidization of the SCLM was likely associated with Phanerozoic subduction zones that surrounded the eastern NCC, implying that oxidization must have been initiated at the base of the SCLM. Given the influence of oxidation on reducing the viscosity of the mantle, destruction of the eastern NCC would have led to the gradual detachment of cratonic materials aided by flow of the asthenosphere. In addition to mantle oxidation, Phanerozoic subduction surrounding the eastern NCC would also have introduced large quantities of water into the mantle, as revealed by the presence of hydrous SCLM-derived lavas in the eastern NCC (Xia et al., 2013; Hong et al., 2017; Ma et al., 2016; this study). This hydration of the SCLM would also have led to a significant decrease in its viscosity, accelerating removal of the cratonic root from the eastern NCC (Niu, 2005; Xia et al., 2013). The destruction of the

eastern NCC probably began during the Late Triassic and attained its climax during the Early Cretaceous (Wu et al., 2005; Yang and Wu, 2009). We suggest that the Mesozoic destruction of the eastern NCC implies that oxidization and rehydration of the SCLM, although beginning during the Paleozoic, were associated primarily with Mesozoic subduction of the Paleo-Pacific oceanic plate (Fig. 9).

Ultramafic lamprophyres and other carbonate-rich rocks are common in other thinned and/or destroyed cratons (e.g., the North Atlantic and Antarctica cratons; Foley, 2008, 2011; Tappe et al., 2017). Because these carbonate-rich rocks are generally synchronous with thinning (Foley, 2008), their appearance indicates the presence of coeval oxidized mantle sources ($\Delta QFM = +0.7$ to $+2.7$; Foley, 2008, 2011; Fig. 7; Table EA3), which contrasts strongly with the highly reduced cratonic root (Foley, 2011; Miller et al., 2016; Fig. 8). The close space–time associations between carbonate-rich igneous rocks and thinned or destroyed cratons suggest that mantle oxidation is probably ubiquitous and plays a crucial role in craton stability.

6. Conclusions

We measured the chemical compositions of high-Fo (Fo > 87) olivine phenocrysts in five Early Cretaceous basalts from the eastern NCC. Taken together, the low temperatures of olivine crystallization (1125 to 1218 °C), the whole-rock compositions, and the extremely low Ti contents (<60 ppm) and high $\delta^{18}O$ (5.8‰–7.2‰) in olivine crystals indicate that the Early Cretaceous basalts originated from the SCLM. Values of fO_2 for the Early Cretaceous basalts and their mantle sources, calculated using D_V values for olivine, are around $\Delta QFM = +1.0$ and $\Delta QFM = +1.5$, respectively. The oxidized Late Mesozoic SCLM beneath the eastern NCC contrasts with the generally reduced nature of cratonic roots worldwide, thus highlighting the important role of redox state in craton destruction. This oxidation was likely caused by ingress of hydrous melts/fluids released by subducting slabs during the Phanerozoic. Both oxidation and rehydration of the SCLM facilitated the thinning and destruction of the eastern NCC.

Supplementary data to this article can be found online at https://doi.org/10.1016/j.gr.2019.11.012.

Declaration of interest

The authors declare that they have no known competing financial interests or personal relationships that could have appeared to influence the work reported in this paper.
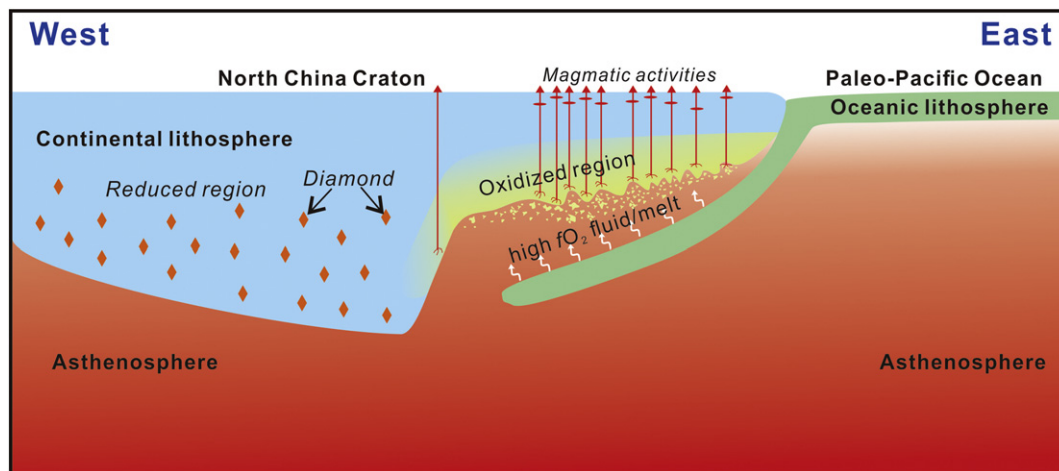
Fig. 9. Schematic diagram illustrating the role of oxidation state on the destruction of the NCC. Paleozoic subduction along the northern, eastern and southern margins of the NCC elevated the fO_2 of the SCLM, but the craton remained stable with limited magmatic activity (e.g., kimberlites) at its margins. Mesozoic subduction of the Paleo-Pacific plate at the eastern margin of the NCC (via release of high-fO_2 fluids/melts; curved white line with arrow in the figure) further oxidized the SCLM, thereby triggering thinning and destruction of the eastern NCC and voluminous magmatic activity.

Acknowledgements

References

Baertschi, P., 1976. Absolute ^{18}O content of standard mean ocean water. Earth Planet. Sci. Lett. 31, 341–344.

Bindeman, I.N., Eiler, J.M., Yogodzinski, G.M., Tatsumi, Y., Stern, C.R., Grove, T.L., Portnyagin, Ma., Hoernle, K., Danyushevsky, L.V., 2005. Oxygen isotope evidence for slab melting in modern and ancient subduction zones. Earth Planet. Sci. Lett. 235, 480–496.

Brounce, M.N., Kelley, K.A., Cottrell, E., 2014. Variations in $Fe^{3+}/Sigma$ Fe of Mariana Arc Basalts and Mantle Wedge fO_2. J. Petrol. 55, 2513–2536.

Brounce, M., Kelley, K.A., Cottrell, E., Reagan, M.K., 2015. Temporal evolution of mantle wedge oxygen fugacity during subduction initiation. Geology 43, 775–778.

Brounce, M., Stolper, E., Eiler, J., 2017. Redox variations in Mauna Kea lavas, the oxygen fugacity of the Hawaiian plume, and the role of volcanic gases in Earth's oxygenation. Proc. Natl. Acad. Sci. 114, 8997–9002.

Canil, D., 2002. Vanadium in peridotites, mantle redox and tectonic environments: Archean to present. Earth Planet. Sci. Lett. 195, 75–90.

Chu, Z.Y., Wu, F.Y., Walker, R.J., Rudnick, R.L., Pitcher, L, Puchtel, I.S., Yang, Y.H., Wilde, S.A., 2009. Temporal evolution of the lithospheric mantle beneath the Eastern North China Craton. J. Petrol. 50, 1857–1898.

Cline, I.I.C.J., Faul, U.H., David, E.C., Berry, A.J., Jackson, I., 2018. Redox-influenced seismic properties of upper-mantle olivine. Nature 555, 355–358.

Cottrell, E., Kelley, K.A., 2011. The oxidation state of Fe in MORB glasses and the oxygen fugacity of the upper mantle. Earth Planet. Sci. Lett. 305, 270–282.

Danyushevsky, L.V., Plechov, P., 2011. Petrolog 3, integrated software for modeling crystallization processes. Geochem. Geophys. Geosyst. 12. https://doi.org/10.1029/2011GC003516.

Dasgupta, R., Hirschmann, M.M., 2006. Melting in the Earth's deep upper mantle caused by carbon dioxide. Nature 440, 659–662.

Dasgupta, R., Hirschmann, M.M., 2010. The deep carbon cycle and melting in Earth's interior. Earth Planet. Sci. Lett. 298, 1–13.

Davis, F.A., Cottrell, E., 2018. Experimental investigation of basalt and peridotite oxybarometers: implications for spinel thermodynamic models and Fe^{3+} compatibility during generation of upper mantle melts. Am. Mineral. 103, 1056–1067.

Eiler, J.M., 2001. Oxygen isotope variations of basaltic lavas and upper mantle rocks. Stable Isotope Geochemistry. Rev. Mineral. Geochem vol. 43, pp. 319–364.

Fan, W.M., Zhang, D.E., Baker, J., Jarvis, K.E., Mason, P.R.D., Menzies, M.A., 2000. On and off the North China Craton, where is the Archaean keel? J. Petrol. 41, 933–950.

Foley, S.F., 2008. Rejuvenation and erosion of the cratonic lithosphere. Nat. Geosci. 1, 503–510.

Foley, S.F., 2011. A reappraisal of Redox melting in the earth's mantle as a function of tectonic setting and time. J. Petrol. 52, 1363–1391.

Foley, S.F., Yaxley, G.M., Rosenthal, A., Buhre, S., Kiseeva, E.S., Rapp, R.P., Jacob, D.E., 2009. The composition of near-solidus melts of peridotite in the presence of CO_2 and H_2O between 40 and 60 kbar. Lithos 112, 274–283.

Foley, S.F., Prelevic, D., Rehfeldt, T., Jacob, D.E., 2013. Minor and trace elements in olivines as probes into Early igneous and mantle melting processes. Earth Planet. Sci. Lett. 363, 181–191.

Gao, S., Rudnick, R.L., Carlson, R.W., McDonough, W.F., Liu, Y.S., 2002. Re-Os evidence for replacement of ancient mantle lithosphere beneath the North China Craton. Earth Planet. Sci. Lett. 198, 307–322.

Gao, S., Rudnick, R.L., Xu, W.L., Yuan, H.L., Liu, Y.S., Walker, R.J., Puchtel, I.S., Liu, X.M., Huang, H., Wang, X.R., Yang, J., 2008. Recycling deep cratonic lithosphere and generation of intraplate magmatism in the North China Craton. Earth Planet. Sci. Lett. 270, 41–53.

Gavrilenko, M., Herzberg, C., Vidito, C., Carr, M.J., Tenner, T., Ozerov, A., 2016. A calcium-in-olivine geohygrometer and its application to subduction zone magmatism. J. Petrol. 57, 1811–1832.

Gazel, E., Plank, T., Forsyth, D.W., Bendersky, C., Lee, C.T.A., Hauri, E.H., 2012. Lithosphere versus asthenosphere mantle sources at the Big Pine Volcanic Field, California. Geochem. Geophys. Geosyst. 13. https://doi.org/10.1029/2012GC004062.

Gonzalez, C.M., Gorczyk, W., 2017. Decarbonation in an intracratonic setting: Insight from petrological-thermomechanical modeling. J. Geophys. Res. Sol. Earth 122, 5992–6013.

Griffin, W.L., Zhang, A.D., O'Reilly, S.Y., Ryan, C.G., 1998. Phanerozoic evolution of the lithosphere beneath the Sino-Korean Craton. In: Flower, M., Chung, S.-L, Lo, C.-H., Lee, T.-Y. (Eds.), Mantle Dynamics and Plate Interactions in East Asia. American Geophysical Union, Washington, DC, pp. 107–126.

Griffin, W.L., O'Reilly, S.Y., Abe, N., Aulbach, S., Davies, R.M., et al., 2003. The origin and evolution of Archean lithospheric mantle. Precamb. Res. 127, 19–41.

Guo, F., Guo, J.T., Wang, C.Y., Fan, W.M., Li, C.W., Zhao, L., Li, H.X., Li, J.Y., 2013a. Formation of mafic magmas through lower crustal AFC processes-an example from the Jinan gabbroic intrusion in the North China Block. Lithos 179, 157–174.

Guo, J.T., Guo, F., Wang, C.Y., Li, C.W., 2013b. Crustal recycling processes in generating the Early Cretaceous Fangcheng basalts, North China Craton: new constraints from mineral chemistry, oxygen isotopes of olivine and whole-rock geochemistry. Lithos 170–171, 1–16.

Herzberg, C., 2011. Identification of source lithology in the Hawaiian and Canary Islands, implications for origins. J. Petrol. 52, 113–146.

Herzberg, C., Asimow, P.D., 2015. PRIMEL3 MEGA.XLSM software for primary magma calculation, peridotite primary magma MgO contents from liquidus to the solidus. Geochem. Geophys. Geosyst. https://doi.org/10.1002/2014GC005631.

Hong, L.B., Xu, Y.G., Ren, Z.Y., Kuang, Y.S., Zhang, Y.L, Li, J., Wang, F.Y., Zhang, H., 2012. Petrology, geochemistry and Re-Os isotopes of peridotite xenoliths from Yantai, Shandong Province, evidence for Phanerozoic lithospheric mantle beneath eastern North China Craton. Lithos 155, 256–271.

Hong, L.B., Zhang, Y.H., Xu, Y.G., Ren, Z.Y., Yan, W., Ma, Q., Ma, L., Xie, W., 2017. Hyrous orthopyroxene-rich pyroxenite source of the Xinkailing high magnesium andesites, Western Liaoning: implications for the subduction-modified lithospheric mantle and the destruction mechanism of the North China Craton. Lithos 282-283, 10–22.

Huang, H., Gao, S., Hu, Z.C., Liu, X.M., Yuan, H.L., 2007. Geochemistry of the high-Mg andesites at Zhangwu, western Liaoning, implication for delamination of newly formed lower crust. Sci. China Earth Sci. 50, 1773–1786.

Irifune, T., Ohuchi, T., 2018. Oxidation softens mantle rocks. Nature 555, 314–315.

Jordan, T.H., 1975. The continental tectosphere. Rev. Geophys. Sp. Phys. 13, 1–12.

Kelemen, P.B., Hanghøj, K., Greene, A.R., 2003. One view of the geochemistry of subduction-related magmatic arcs, with an emphasis on primitive andesite and lower crust. Treatise Geochem. 3, 593–659. https://doi.org/10.1016/B0-08-043751-6/03035-8.

Kelley, K.A., Cottrell, E., 2012. The influence of magmatic differentiation on the oxidation state of Fe in a basaltic arc magma. Earth Planet. Sci. Lett. 329, 109–121.

Kress, V.C., Carmichael, I.S.E., 1988. Stoichiometry of the iron oxidation reaction in silicate melts. Am. Mineral. 73, 11–12.

Kress, V.C., Carmichael, I.S.E., 1991. The compressibility of silicate liquids containing Fe_2O_3 and the effect of composition, temperature, oxygen fugacity and pressure on their redox states. Contrib. Mineral. Petrol. 108, 82–92.

Kuang, Y.S., Pang, C.J., Luo, Z.Y., Hong, L.B., Zhong, Y.T., Qiu, H.N., Xu, Y.G., 2012. ^{40}Ar-^{39}Ar geochronology and geochemistry of mafic rocks from Qingshan Group, Jiaodong area: implications for the destruction of the North China Craton. Acta Petrol. Sin. 28, 1073–1091 (In Chinese with English abstract).

Le Bas, M.J., Maitre, R.W.L., Streckeisen, A., Zanettin, B., 1986. A chemical classification of volcanic rocks based on the total alkali-silica diagram. J. Petrol. 27, 745–750.

Lee, C.-T., Luffi, A.P., Plank, T., Dalton, H., Leeman, W.P., 2009. Constraints on the depths and temperatures of basaltic magma generation on Earth and other terrestrial planets using new thermobarometers for mafic magmas. Earth Planet. Sci. Lett. 279, 20–33.

Lee, C.T.A., Luffi, P., Chin, E.J., 2011. Building and destroying continental mantle. Annu. Rev. Earth Planet. Sci. 39, 59–90.

Liu, D.-Y., Nutman, A.P., Compston, W., Wu, J.S., Shen, Q.-H., 1992. Remnants of N3800 Ma crust in the Chinese part of the Sino-Korean craton. Geology 20, 339–342.

Liu, Y.S., Hu, Z.C., Gao, S., Gunther, D., Xu, J., Gao, C.G., Chen, H.H., 2008. In situ analysis of major and trace elements of anhydrous minerals by LA-ICP-MS without applying an interalstandard. Chem. Geol. 257, 34–43.

Ma, Q., Xu, Y.G., Zheng, J.P., Griffin, W.L., Hong, L.B., Ma, L., 2016. Coexisting early Cretaceous high-Mg andesites and adakitic rocks in the North China Craton: the role of water in interaplate magmatism and cratonic destruction. J. Petrol. 57, 1279–1308.

McDonough, W.F., Sun, S.S., 1995. The composition of the Earth. Chem. Geol. 120, 223–253.

Médard, E., Grove, T.L., 2008. The effect of H_2O on the olivine liquidus of basaltic melts, experiments and thermodynamic models. Contrib. Mineral. Petrol. 155, 417–432.

Menzies, M.A., Xu, Y.G., 1998. Geodynamics of the North China Craton. In: Flower, M.F.J., Chung, S., Lo, C., Lee, T. (Eds.), Mantle Dynamics and Plate Interactions in East Asia. Am. Geophy. Union, Geodyn. Ser vol. 27, pp. 155–165.

Menzies, M.A., Fan, W.M., Zhang, M., 1993. Palaeozoic and Cenozoic lithoprobes and the loss of N120 km of Archaean Lithosphere, Sino-Korean craton, China. Geol. Soc. London, Special Pub. 76, 71–81.

Miller, W.G.R., Holland, T.J.B., Gibson, S.A., 2016. Garnet and spinel oxybarometers: new internally consistent multi-equilibria models with applications to the oxidation state of the lithospheric mantle. J. Petrol. 57 (1199–1122).

Niu, Y.L., 2005. Generation and evolution of basaltic magmas: some basic concepts and a new view on the origin of Mesozoic-Cenozoic basaltic volcanism in Eastern China. Geol. J. China Univ. 11, 9–46.

Pang, C.J., Wang, X.C., Xu, Y.G., Wen, S.N., Kuang, Y.S., Hong, L.B., 2015. Pyroxenite-derived Early Cretaceous lavas in the Liaoning Peninsula: implication for metasomatism and thinning of the lithospheric mantle beneath North China Craton. Lithos 227, 77–93.

Peslier, A.H., Woodland, A.B., Bell, D.R., Lazarov, M., 2010. Olivine water contents in the continental lithosphere and the longevity of cratons. Nature 467, 78–81.

Plank, T., Forsyth, D.W., 2016. Thermal structure and melting conditions in the mantle beneath the Basin and Range province from seismology and petrology. Geochem. Geophys. Geosyst. 17, 1312–1338.

Pu, X.F., Lange, R.A., Moore, G., 2017. A comparison of olivine-melt thermometers based on D_{Mg} and D_{Ni}: the effects of melt composition, temperature, and pressure with applications to MORBs and hydrous arc basalts. Am. Mineral. 102, 750–765.

Qiang, S.P., Ren, Z.Y., Richard, W., Zhang, L., Zhang, Y.H., Hong, L.B., Ding, X.L., Wu, Y.D., 2017. Petrogenesis of Early Cretaceous basaltic lavas from the North China Craton: implications for the cratonic destruction. J. Geophys. Res. Solid Earth https://doi.org/10.1002/2016JB013548.

Rielli, A., Tomkins, A.G., Nebel, O., Brugger, J., Etschmann, B., Paterson, D., 2018. Garnet peridotites reveal spatial and temporal changes in the oxidation potential of subduction. Sci. Rep. 8. https://doi.org/10.1038/s41598-018-34669-0.

Stagno, V., Ojwang, D.O., McCammon, C.A., Frost, D.J., 2013. The oxidation state of the mantle and the extraction of carbon from Earth's interior. Nature 493, 84–88.

Su, B.X., Gu, X.Y., Deloule, E., Zhang, H.F., Li, Q.L., Li, X.H., Vigier, N., Tang, Y.J., Tang, G.Q., Liu, Y., Brewer, A., Mao, Q., Ma, Y.G., 2015. Potential orthopyroxene, clinopyroxene and olivine reference materials for in situ lithium isotope determination. Geostand. Geoanal. Res. 39, 357–369.

Tappe, S., Romer, R.L., Stracke, A., Steenfelt, A., Smart, K.A., Muehlenbachs, K., Torsvik, T.H., 2017. Sources and mobility of carbonate melts beneath cratons, with implications for deep carbon cycling, metasomatism and rift initiation. Earth Planet. Sci. Lett. 466, 152–167.

Thompson, R.N., Gibson, S.A., 2000. Transient high temperatures in mantle plume heads inferred from magnesian olivines in Phanerozoic picrites. Nature 407, 502–506.

Toplis, M.J., 2005. The thermodynamics of iron and magnesium partitioning between olivine and liquid: criteria for assessing and predicting equilibrium in natural and experimental systems. Contrib. Mineral. Petrol. 149, 22–39.

Walker, R.J., Carlson, R.W., Shirey, S.B., Boyd, F.R., 1989. Os, Sr, Nd, and Pb isotope systematics of southern African peridotite xenoliths: implications for the chemical evolution of subcontinental mantle. Geochim. Cosmochim. Acta 53, 1583–1595.

Wang, W., Takahashi, E., Sueno, S., 1998. Geochemical properties of lithospheric mantle beneath Sino-Korea craton: evidence from garnet xenocrysts and diamond inclusions. Phys. Earth Planet. Inter. 107, 249–260.

Wang, C.G., Xu, W.L., Yang, D.B., Liu, Y.S., Pei, F.P., Li, Q.L., Zhou, Q.J., 2018. Olivine oxygen isotope evidence for intra-continental recycling of delaminated continental crust. Geochem. Geophys. Geosyst. 19, 1913–1924.

Windley, B.F., Maruyama, S., Xiao, W.J., 2010. Delamination/thinning of sub-continental lithospheric mantle under Eastern China, the role of water and multiple subduction. Am. J. Sci. 310, 1250–1293.

Wu, F.Y., Lin, J.Q., Wilde, S.A., Zhang, X.O., Yang, J.H., 2005. Nature and significance of the Early Cretaceous giant igneous event in eastern China. Earth Planet. Sci. Lett. 233, 103–119.

Wu, F.Y., Xu, Y.G., Zhu, R.X., Zhang, G.W., 2014. Thinning and destruction of the cratonic lithosphere, a global perspective. Sci. China Ser. D Earth Sci. 57, 2878–2890.

Xia, Q.K., Liu, J., Liu, S.C., Kovacs, I., Feng, M., Dang, L., 2013. High water content in Mesozoic primitive basalts of the North China Craton and implications on the destruction of cratonic mantle lithosphere. Earth Planet. Sci. Lett. 361, 85–97.

Xu, Y.G., 2001. Thermo-tectonic destruction of the Archean lithospheric keel beneath the Sino-Korean Craton in China: evidence, timing and mechanism. Phys. Chem. Earth (A) 26, 747–757.

Xu, Y.G., Li, H.Y., Pang, C.J., He, B., 2009. On the timing and duration of the destruction of the North China Craton. Chin. Sci. Bull. 54. https://doi.org/10.1007/s11434-009-0346-5.

Xu, W.L., Zhou, Q.J., Pei, F.P., Yang, D.B., Gao, S., Li, Q.L., Yang, Y.H., 2013. Destruction of the North China Craton: delamination or thermal/chemical erosion? Mineral chemistry and oxygen isotope insights from websterite xenoliths. Gondwana Res. 23, 119–129.

Yan, G.H., Mu, B.L., Zeng, Y.S., Cai, J.H., Ren, K.X., Li, F.T., 2007. Igneous carbonatites in North China Craton: the temporal and spatial distribution, Sr and Nd isotopic characteristics and their geological significance. Geol. J. China Univ. 13, 463–473 (in Chinese with English abstract).

Yang, J.H., Wu, F.Y., 2009. Triassic magmatism and its relation to decratonization in the eastern North China Craton. Sci. China Ser. D: Earth Sci 52, 1319–1330.

Yang, Q., Xia, X.P., Zhang, W.F., Zhang, Y.Q., Xiong, B.Q., Xu, Y.G., Wang, Q., Wei, G.J., 2018. An evaluation of precision and accuracy of SIMS oxygen isotope analysis. Sol. Earth Sci. 3, 81–86.

Ying, J.F., Zhou, X., Zhang, H.F., 2004. Geochemical and isotopic investigation of the Laiwu-Zibo carbonatites from western Shandong Province, China, and implications for their petrogenesis and enriched mantle source. Lithos 75, 413–426.

Zhang, H.F., Sun, M., Zhou, X.H., Fan, W.M., Zhai, M.G., Yin, J.F., 2002. Mesozoic lithosphere destruction beneath the North China Craton: evidence from major-, trace-element and Sr-Nd-Pb isotope studies of Fangcheng basalts. Contrib. Mineral. Petrol. 144, 241–253.

Zhang, L., Ren, Z.Y., Xia, X.P., Yang, Q., Hong, L.B., Wu, D., 2018. In situ determination of trace elements in melt inclusions using laser ablation–inductively coupled plasma-sector field-mass spectrometry. Rapid Commun. Mass Spectrom. https://doi.org/10.1002/rcm.8359.

Zhao, G.C., Wilde, S.A., Cawood, P.A., Sun, M., 2001. Archean blocks and their boundaries in the North China Craton, lithological, geochemical, structural and P-T path constraints and tectonic evolution. Precambrian Res. 107, 45–73.

Zheng, J.P., Griffin, W.L., O'Reilly, S.Y., Lu, F.X., Wang, C.Y., Zhang, M., Wang, F.Z., Li, H.M., 2004. 3.6 Ga lower crust in central China: new evidence on the assembly of the North China Craton. Geology 32, 229–232.

Zheng, J.P., Griffin, W.L., O'Reilly, S.Y., Yang, J.S., Li, T.F., Zhang, M., Zhang, R.Y., Liou, J.G., 2006. Mineral chemistry of peridotites from Paleozoic, Mesozoic and Cenozoic lithosphere: constraints on mantle evolution beneath Eastern China. J. Petrol. 47, 2233–2256.

Zheng, Y.F., Xu, Z., Zhao, Z.F., Dai, L.Q., 2018. Mesozoic mafic magmatism in North China: implications for thinning and destruction of cratonic lithosphere. Sci. China Earth Sci. 61, 353–385.

Zhou, J.Q., Xu, W.L., Yang, D.B., Pei, F.P., Wang, W., Yuan, H.L., Gao, S., 2012. Modification of the lithospheric mantle by melt derived from recycled continental crust evidenced by wehrlite xenoliths in Early Cretaceous high-Mg diorites from western Shandong, China. Sci. China Earth Sci. 55, 1972–1986.

Zhu, R., Yang, J., Wu, F., 2012. Timing of destruction of the North China Craton. Lithos 149, 51–60.

Zong, K.Q., Liu, Y.S., 2018. Carbonate metasomatism in the lithospheric mantle: implications for cratonic destruction in North China. Sci. China Earth Sci. 61, 711–729.

Zong, K.Q., Klemd, R., Yuan, Y., He, Z.Y., Guo, J.L., Shi, X.L., Liu, Y.S., Hu, Z.C., Zhang, Z.M., 2017. The assembly of Rodinia: the correlation of Early Neoproterozoic (ca. 900 Ma) high grade metamorphism and continental arc formation in the southern Beishan Orogen, southern Central Asian Orogenic Belt (CAOB). Precambrian Res. 290, 32–48.